PHYSICAL REVIEW B **84**, 165112 (2011)

Anatomy of the self-energy

B. Sriram Shastry
Physics Department, University of California, Santa Cruz, California 95064, USA
(Received 13 April 2011; published 11 October 2011)

The general problem of representing the Greens function $G(k,z)$ in terms of self-energy in field theories lacking Wick's theorem is considered. A simple construction shows that a Dyson-like representation with a self-energy $\Sigma(k,z)$ is always possible, provided we start with a spectral representation for $G(k,z)$ for finite-sized systems and take the thermodynamic limit. The self-energy itself can then be iteratively expressed in terms of another higher order self-energy, capturing the spirit of Mori's formulation. We further discuss alternative and more general forms of $G(k,z)$ that are possible. In particular, a recent theory, by the author, of extremely correlated Fermi liquids at density n, for Gutzwiller projected noncanonical Fermi operators, obtains a new form of the Greens function: $G(k,z) = [(1-\frac{n}{2}) + \Psi(k,z)]/[z - \hat{E}_k - \Phi(k,z)]$, with a pair of self-energies $\Phi(z)$ and $\Psi(z)$. Its relationship with the Dyson form is explored. A simple version of the two-self-energies model was shown recently to successfully fit several data sets of photoemission line shapes in cuprates. We provide details of the unusual spectral line shapes that arise in this model, with the characteristic skewed shape depending upon a single parameter. The energy distribution curve (EDC) and momentum distribution curve (MDC) line shapes are shown to be skewed in opposite directions, and provide a testable prediction of the theory.

DOI: 10.1103/PhysRevB.84.165112 PACS number(s): 79.60.−i

I. INTRODUCTION

Our work explores the representation of the Greens function $G(k,z)$ of a particle in field theories without Wick's theorem. While Wick's theorem for bosons and fermions automatically gives rise to the Dyson form of self-energy, its absence for noncanonical, i.e., general operators (other than bosons of fermions), leads to a conundrum that is poorly understood. This work addresses a particular type of noncanonical theory originating from Gutzwiller projection of electrons on a lattice.

The representation of the propagator or the Greens function in terms of its Dyson self-energy is a fundamental paradigm of standard interacting relativistic and nonrelativistic field theories. The structure of this representation and the generation of approximations for the self-energy in terms of Feynman diagrams, the vertex function, or higher order Greens functions form the dominant part of existing literature of many-particle physics.

In the context of extending these studies to extremely large and singular repulsive interactions, termed extreme correlations,[1] one needs to deal with noncanonical electrons. A standard noncanonical problem involves the Hubbard operators[2] $X_j^{a,b}$ located at sites j of a lattice. These are "graded" projection operators with label a representing the three allowed local configurations 0, $\uparrow$, and $\downarrow$. Among these operators, $X_j^{0\sigma}$ and $X_j^{\sigma 0}$ are fermionic destruction- and creation-type objects. Their Greens function is measured directly in angle-resolved photoemission experiments (ARPES) on certain experimental systems embodying extreme correlations, including the high-temperature superconductors.[3]

Quite recently, the author has formulated in Ref. 1, the theory of an extremely correlated Fermi liquid (ECFL) state of the t-J model, where he has found another type of representation for the Greens function with a pair of self-energies [see Eq. (4) below] by using the nonperturbative Schwinger approach of source fields to depict the equations of motion. The use of more general forms of Greens functions is not completely new, there are examples in literature of multiple self-energies in Refs. 4 and 5. The physics of extreme correlations treated here is based on nonperturbative considerations without obvious parallels in weak or intermediate coupling problems. It leads to the two-self-energies form, Eq. (4), whose distinctive signatures are strikingly different from those of Fermi liquids.

The technical details of the construction in Ref. 1 are intricate and require the processing of two parallel hierarchies for the two self-energies. A separate paper is in preparation detailing the involved technical details and the calculation in Ref. 1. Further background details of the notation, definitions, and sum rules satisfied by the Greens functions for extreme correlations, and its analyticity can be found in the earlier publication.[2] A suggestive functional form of the Greens function, Eq. (37), emerges from Ref. 1, by making the assumption of momentum independence of the two self-energies, valid in high dimensions. It satisfies the number sum rule and the total particle weight integrates to unity in each state. In Ref. 3, Gweon, Gu, and the author have shown that several experimental data sets on ARPES by different groups using both the traditional synchrotron light source and a laser light source can be reconciled very well with the line shape in Eqs. (37) and (60). This is the first satisfactory functional form that has been found to fit both laser and synchrotron data and to work very well with few adjustable parameters.

Therefore a major objective of this paper is to elucidate the detailed form of the spectral lines that emerged from the above simple version of the ECFL theory in Ref. 1 and successfully employed to understand experiments in Ref. 3. Our hope is that this detailed analysis will familiarize readers with the nuances of the new spectral function, and thereby facilitate ARPES line-shape analysis of further experiments on high-temperature superconductors and other materials, in a manner analogous to that in Ref. 3.

For the above purpose, we recall that in a lattice of finite (say small) number of sites, the state space is finite dimensional and hence the Greens function for arbitrarily complicated objects can be computed by numerical means, leading to rational functions of the complex frequency z as in Eq. (5) below.

We begin by studying this representation and see how the Dyson representation arises; we find that the two-self-energies representation, Eq. (4), is also quite natural from this view point. We further study the infinite size limits where the poles coalesce to give cuts in the complex z plane. We adopt a phenomenological model for an underlying auxiliary Fermi liquid (aux-FL) self-energy, enabling us to display analytic expressions for the Greens function. We provide a detailed perspective on the representation in Eq. (37), namely, the location of the poles and the subtle differences from a standard Fermi liquid.

Another result in this paper is to show that a Dyson-like representation with a self-energy $\Sigma(k,z)$ is always possible, provided we start with a spectral representation. The self-energy itself can then be iteratively expressed in terms of another higher order self-energy. This hierarchical result is cast in the same form as the Mori formalism. While the Mori formalism is very abstract, and expressed in terms of projection operators, we can go beyond it in a certain sense. By working with standard spectral representation, we show that it is possible to express the higher self-energy spectral functions in terms of the lower ones, leading to an explicit hierarchy. Our construction completely bypasses the Mori projection operators, and should be useful in throwing light on the latter.

The plan of the paper is as follows. In Secs. II and III, we note the spectral representation and study the Greens function as a rational function of complex frequency z for a finite system. In Sec. IV, we note the representation in the limit of infinite size and introduce the high-dimensional expression with two self-energies. The detailed structure of the characteristic line shape as in Eq. (60) is discussed, and its dependence on physical parameters displayed with the help of a numerical example. An explicit example of the auxiliary Fermi-liquid Greens function is provided, and typical values of the parameters are argued for. In Sec. V, the line shapes in EDC and MDC are displayed in detail, in order to bring out the specific signatures of the theory, namely, a skew in the spectrum arising from the caparison factor in Ref. 1 and Eq. (37). In Sec. VI, we discuss the amusing connection with higher order self-energies of the type that Mori's formalism yields, but at a much more explicit level than what is available in the literature.

II. SPECTRAL REPRESENTATION OF THE GREENS FUNCTION

Let us begin with the spectral representation[10] of the Matsubara Greens function at finite temperatures given by

$$G(k,z) = \int dx \, \frac{\rho_G(k,x)}{z-x}, \tag{1}$$

where G is the Greens function at a fixed wave vector k, ρ_G is its spectral density, and the integration range is $-\infty \leqslant x \leqslant \infty$. To simplify notation, we call the Greens function as $G(k,z)$, the same object was denoted by $\mathcal{G}(k,z)$ in Ref. 1. The index k can be also replaced by a spatial index when dealing with a local Greens function. The spectral function $\rho_G(k,x)$ in most problems of interest in condensed matter physics has a compact support, so that $G(k,z)$ has "reasonable" behavior in the complex z plane, with an asymptotic $1/z$ fall off, and, apart from a branch cut on a portion of the real line, it is analytic. The frequency z is either fermionic or bosonic depending on the statistics of the underlying particles. The spectral function is given by the standard formula[2,10]

$$\rho_G(k,x) = \sum_{\alpha,\beta} |\langle\alpha|A(k)|\beta\rangle|^2 (p_\alpha + p_\beta)\, \delta(x+\varepsilon_\alpha - \varepsilon_\beta), \tag{2}$$

where $A(k)$ is the destruction operator, p_α is the Boltzmann probability of the state α given by $e^{-\beta\varepsilon_\alpha}/Z$, and ε_α is the eigenvalue of the grand Hamiltonian of the system $K = H - \mu\hat{N}$. In the case of canonical particles, $A(k)$ is the usual Fermi or Bose destruction operator. In Ref. 1, noncanonical Hubbard 'X operators are considered; we will not require any detailed information about them here except that the anticommutator $\{A, A^\dagger\}$ is not unity, but rather an object with a known expectation value $(1 - n/2)$, in terms of the dimensionless particle density n.

We consider two alternate representations of the Greens function in terms of the complex frequency z that are available in many-body physics: (a) for canonical bosons or fermions, the Dyson representation in terms of a single self-energy $\Sigma(z)$ and (b) for noncanonical particles, a novel form proposed recently by the author with two self-energy type objects $\Phi(z)$ and $\Psi(z)$:

$$G(k,z) = \frac{a_G}{z - \hat{E}_k - \Sigma(k,z)} \quad \text{(Dyson)} \tag{3}$$

$$= \frac{a_G + \Psi(k,z)}{z - \hat{E}_k - \Phi(k,z)} \quad \text{(ECFL)}. \tag{4}$$

For canonical objects, $a_G = 1$ and for Hubbard operators in the ECFL we write $a_G = 1 - n/2$. We start below from a finite-size system, where the Greens function is a meromorphic function expressible as the sum over isolated poles in the complex frequency plane with given residues. In fact, it is a rational function as well, expressible as the ratio of two polynomials. Using simple arguments, we will see that the above two representations in Eqs. (3) and (4) are both natural ways of proceeding with the self-energy concept. In the limit of a large system, the poles coalesce to give us cuts in the complex frequency plane with specific spectral densities. In this limit, we display the equations relating the different spectral functions.

III. FINITE-SYSTEM GREENS FUNCTION

We drop the explicit mention of the wave vector k, and start with the case of a finite-sized system, where we may diagonalize the system exactly and assemble the Greens function from the matrix elements of the operators A and the eigenenergies as in Eq. (2). We see that ρ_G is a sum over say m delta functions located at the eigenenergies E_j (assumed distinct), so we can write the meromorphic representation

$$\bar{G}(z) = \sum_{j=1}^{m} \frac{a_j}{z - E_j}. \tag{5}$$

The overbar in $\bar{G}(z)$ is to emphasize that we are dealing with the finite-sized version of the Greens function $G(z)$. Here, a_j and E_j constitute $2m$ known real parameters. The sum

$$\sum_{j=1}^{m} a_j = a_G, \tag{6}$$

where $a_G = 1$ for canonical objects and we denote $a_G = 1 - n/2$ for the noncanonical case of ECFL. In the infinite-size limit, we set $\bar{G}(z) \to G(z)$. It is clear that for $z \gg \{E_j\}_{\max}$, we get the asymptotic behavior $\bar{G} \to \frac{a_G}{z}$, and therefore $\bar{G}$ is a rational function that may be expressed as the ratio of two polynomials in z of degrees $m-1$ and m:

$$\bar{G}(z) = a_G \frac{P_{m-1}(z)}{Q_m(z)}, \quad Q(z) = \prod_{j=1}^{m}(z - E_j),$$
$$P(z) = \prod_{r=1}^{m-1}(z - \gamma_r), \tag{7}$$

where the roots γ_r are expressible in terms of a_j and E_j. We use the convention that all polynomials Q_m have the coefficient of the leading power of z as unity, and the degree is indicated explicitly.

We now proceed to find the self-energy type expansion for $\bar{G}$, and for this purpose, multiplying Eq. (5) by z and rearranging we get the "equation of motion:'

$$(z - \hat{E})\bar{G}(z) = a_G + \bar{I}(z), \tag{8}$$

where we introduced a mean energy $\hat{E}$:

$$\hat{E} = \frac{1}{a_G}\sum a_j E_j,$$
$$\bar{I}(z) = \sum_{j=1}^{m} \frac{a_j(E_j - \hat{E})}{z - E_j}, \tag{9}$$

so that asymptotically at large z we get $\bar{I}(z) \sim O(1/z^2)$. In standard theory, $\hat{E}$ plays the role of the Hartree-Fock self-energy so that the remaining self-energy vanishes at high frequencies.[12] Motivated by the structure of the theory of extremely correlated Fermi systems,[1] we next introduce the basic decomposition

$$\bar{I}(z) = \bar{G}(z)\Phi(z) + \Psi(z), \tag{10}$$

where we have introduced two self-energy type functions $\Phi(z)$ and $\Psi(z)$ that will be determined next. Clearly, Eq. (10) leads immediately to the Greens function (4) (or Eq. (3), if we set $\Psi \to 0$). The rationale for Eq. (10) lies in the fact that the function $\bar{I}$ has the same poles as $\bar{G}(z)$. Thus it has a representation as a ratio of two polynomials:

$$\bar{I}(z) = i_0 \frac{R_{m-2}(z)}{Q_m(z)}, \tag{11}$$

with R_{m-2} a polynomial of degree $m-2$, i_0 a suitable constant, and the same polynomial Q from Eq. (7), thereby it is natural to seek a proportionality with $\bar{G}$ itself. If we drop Ψ and rename $\Phi \to \Sigma$, then this gives the usual Dyson self-energy $\Sigma(z)$ determined uniquely using Eqs. (7) and (11) as

$$\Sigma(z) = \frac{i_0}{a_G}\frac{R_{m-2}(z)}{P_{m-1}(z)}. \tag{12}$$

Expression (10) offers a more general possibility, where $\Phi(z)$ and $\Psi(z)$ may be viewed as the quotient and remainder obtained by dividing $\bar{I}(z)$ by $\bar{G}(z)$. It is straightforward to see that $\Psi(z)$ and $\Phi(z)$ are also rational functions expressible as ratios of two polynomials:

$$\Psi(z) = \psi_o \frac{K_{m-3}(z)}{D_{m-1}(z)}, \quad \Phi(z) = \phi_o \frac{L_{m-2}(z)}{D_{m-1}(z)}, \tag{13}$$

where K, L, and D are polynomials of the displayed degree. Comparing the poles and the zeros of $\bar{G}$ in Eq. (4) with Eqs. (12) and (7), we write down two equations:

$$a_G P_{m-1} = a_G D_{m-1} + \psi_o K_{m-3},$$
$$Q_m = (z - \bar{E})D_{m-1} - \phi_0 L_{m-2}, \tag{14}$$

so that we may eliminate D and write an identity,

$$(z - \bar{E})P_{m-1} - Q_m = \frac{\psi_o}{a_G}(z - \bar{E})K_{m-3} + \phi_o L_{m-2}. \tag{15}$$

Here, the left-hand side is assumed known and we have two polynomials to determine from this equation. Therefore there are multiple solutions of this problem, and indeed setting $K \to 0$ gives the Dyson form as a special case.

A. A simple example with two sites

The Greens function of the t-J model at density n with $J = 0$ and only two sites is a trivial problem that illustrates the two possibilities discussed above. The two quantum numbers $k = 0, \pi$ correspond to the bonding and antibonding states with energies $e_k = \mp t$, and a simple calculation at a given k gives Eq. (5) as

$$\bar{G}(k,z) = \frac{a_1}{z - e_k} + \frac{a_2}{z + e_k}, \tag{16}$$

where $z = i\omega_n + \mu$, $a_2 = e^{\beta\mu}[1 + e^{\beta(\mu - e_k)}]/(2Z)$, $a_1 = 1 - n/2 - a_2$, and the grand partition function $Z = 1 + 4e^{2\beta\mu} + 4e^{\beta\mu}\cosh(\beta t)$. This can be readily expressed as

$$\bar{G}(k,z) = \frac{\left(1 - \frac{n}{2}\right) + \Psi(k,z)}{z - E_k - \Phi(k,z)}, \quad \Psi(k,z) = \frac{B_k}{z + E_k},$$
$$\Phi(k,z) = \frac{A_k}{z + E_k}, \tag{17}$$

where E_k is arbitrary, $A_k = (E_k^2 - e_k^2)$, and $B_k = (1 - n/2)(\bar{E}_k - E_k)$ and with the first moment of energy $\bar{E}_k = e_k(a_1 - a_2)/(1 - n/2)$. As we expected, the functions Ψ, Φ thus have a single pole, as opposed to $\bar{G}$ with two poles. In this case the dynamics is rather trivial, so that the choice of E_k is free. If we set $E_k = \bar{E}_k$, the residue B_k vanishes and so the second form collapses.

B. Summary of analysis

In summary, guided by analyticity and the pole structure of $\overline{G}(k,z)$, we find it possible to go beyond the standard Dyson representation. However, we end up getting more freedom than we might have naively expected. This excess freedom is not unnatural, since we haven't yet discussed the microscopic origin of these two self-energies. The theory in Ref. 1 provides

an explicit expression for the two objects Ψ and Φ, where a common linear functional differential operator $\mathbf{L}$ generates these self-energies by acting upon different "seed" functions as in Eq. (7) of Ref. 1. The above discussion therefore provides some intuitive understanding of the novel form of the Greens function in Eq. (4), without actually providing an alternative derivation to that in Ref. 1.

IV. INFINITE-SYSTEM SPECTRAL DENSITIES AND RELATIONSHIPS

In the infinite-size limit, the various functions will be represented in terms of spectral densities obtained from the coalescing of the poles. Following Eq. (1), we will denote a general function

$$Q(z) = \int dx \, \frac{\rho_Q(x)}{z - x}, \tag{18}$$

where $Q = \Sigma, \Phi, \Psi$ in terms of its density $\rho_Q(x)$. The density is given by $\rho_Q(x) = (-\frac{1}{\pi})\Im m \, Q(x + i0^+)$, as usual. In parallel to the discussion of Eq. (1), the assumption of a compact support of ρ_Q gives us well-behaved functions. We now turn to the objective of relating the spectral functions in the two representations discussed above.

A. Spectral representation for the Dyson self-energy

Let us start with Eq. (1) and the standard Dyson form (3) where we drop the overbar and study the infinite system function $G(z)$. We use the symbolic identity:

$$\frac{1}{x + i0^+} = \mathcal{P}\frac{1}{x} - i\pi\delta(x), \tag{19}$$

with real x, $\mathcal{P}$ denoting the principal value, and the Hilbert transform of a function $f(u)$ is defined by

$$\mathcal{H}[f](x) = \mathcal{P}\int_{-\infty}^{\infty} dy \, \frac{f(y)}{x - y}. \tag{20}$$

We note the following standard result for completeness:

$$\rho_G(x) = a_G \, \frac{\rho_\Sigma(x)}{[\pi\rho_\Sigma(x)]^2 + [x - \hat{E} - \mathcal{H}[\rho_\Sigma](x)]^2}. \tag{21}$$

A more interesting inverse problem is to solve for $\rho_\Sigma(x)$ given $G(z)$. Toward this end, we rewrite the Dyson equation as

$$\Sigma(z) = z - \hat{E} - \frac{a_G}{G(z)}, \tag{22}$$

where the self-energy vanishes asymptotically as $1/z$, provided the constant part, if any, is absorbed in $\hat{E}$. Therefore this object can be decomposed in the fashion of Eq. (18). We compare Eq. (22) with Eq. (18) with $Q \to \Sigma$ and conclude that

$$\rho_\Sigma(x) = \frac{1}{\pi}\Im m \, \frac{a_G}{G(x + i0^+)} = \frac{a_G \, \rho_G(x)}{[\pi\rho_G(x)]^2 + [\Re e \, G(x)]^2}. \tag{23}$$

The real part can be found either by taking the Hilbert transform,

$$\Re e \, \Sigma(x) = \mathcal{H}[\rho_\Sigma](x), \tag{24}$$

or more directly as

$$\begin{aligned} \Re e \, \Sigma(x) &= x - \hat{E} - \Re e \, \frac{a_G}{G(x + i0^+)} \\ &= x - \hat{E} - \frac{a_G \, \Re e \, G(x)}{[\pi\rho_G(x)]2 + [\Re e \, G(x)]^2}. \end{aligned} \tag{25}$$

B. Spectral representation for the ECFL self-energies

For the ECFL Greens function in Eq. (4), we set $a_G = (1 - \frac{n}{2})$ and write $\hat{E} \to \xi$ representing the single-particle energy measured from the chemical potential. We start with the expression:

$$G(\xi, z) = \frac{1}{z - \xi - \Phi(z)} \times \left[\left(1 - \frac{n}{2}\right) + \Psi(z)\right], \tag{26}$$

and express it in terms of the two spectral functions ρ_Ψ and ρ_Φ.[13] We can write spectral function ρ_G:

$$\begin{aligned} \rho_G(\xi, x) = &\frac{\rho_\Phi(x)}{[\pi\rho_\Phi(x)]^2 + [x - \xi - \mathcal{H}[\rho_\Phi](x)]^2} \\ &\times \left[\left(1 - \frac{n}{2}\right) + \frac{\xi - x}{\Delta(\xi, x)} + \eta(\xi, x)\right], \end{aligned} \tag{27}$$

where $\Delta(\xi, x)$ and the term η are defined as

$$\Delta(\xi, x) = -\frac{\rho_\Phi(\xi, x)}{\rho_\Psi(\xi, x)}, \tag{28}$$

$$\eta(\xi, x) = \mathcal{H}[\rho_\Psi](\xi, x) + \frac{1}{\Delta(\xi, x)}\mathcal{H}[\rho_\Phi](\xi, x). \tag{29}$$

The real part of G is also easily found as

$$\Re e \, G(\xi, x) = \frac{\left[\left(1 - \frac{n}{2}\right) + \mathcal{H}[\rho_\Psi](\xi, x)\right][x - \xi - \mathcal{H}[\rho_\Phi](\xi, x)] - \pi^2\rho_\Psi(\xi, x)\rho_\Phi(\xi, x)}{[\pi\rho_\Phi(\xi, x)]^2 + [x - \xi - \mathcal{H}[\rho_\Phi](\xi, x)]^2}. \tag{30}$$

Thus given the ECFL form of the Greens function, we can calculate the Dyson Schwinger form of self-energy in a straightforward way using the inversion formula, Eqs. (23) and (24). The inverse problem of finding Φ and Ψ from a given Σ or G is expected to be ill defined, as discussed above for finite systems.

The first Fermi liquid (FL) factor in Eq. (27) has a peak at the Fermi-liquid quasiparticle frequency $E_k^{\rm FL}$ for a given ξ_k given as the root of

$$E_k^{\rm FL} - \xi_k - \mathcal{H}[\rho_\Phi]\left(\xi_k, E_k^{\rm FL}\right) = 0, \tag{31}$$

however, ρ_G itself has a slight shift in the peak due to the linear-x dependence in the numerator. This is analyzed in detail in the next section for a model self-energy. At this solution $x(\xi)$, Eq. (30) gives a relation:

$$\rho_\Psi\left(\xi_k, E_k^{\rm FL}\right) = -\rho_\Phi\left(\xi_k, E_k^{\rm FL}\right) \times \Re e\; G\left(\xi_k, E_k^{\rm FL}\right). \tag{32}$$

C. High-dimensional ECFL model with $\vec{k}$-independent self-energies and its Dyson representation

In this section, we illustrate the two self-energies and their relationships in the context of the recent work on the ECFL of Ref. 1, and in Ref. 3. Here, we study a model Greens function, proposed in Ref. 1 for the t-J model, that should be suitable in high enough dimensions. It is sufficiently simple so that most calculations can be done analytically. The model Greens function satisfies the Luttinger-Ward sum rule[6] and thereby maintains the Fermi surface of the Fermi gas, but yields spectral functions that are qualitatively different from the Fermi liquid. This dichotomy is possible since it corresponds to a simple approximation within a formalism that is very far from the standard Dyson theory, as explained in the previous sections. Our aim in this section is to take this model Greens function of the ECFL and to express it in terms of the Dyson self-energy so as to provide a greater feel for the model.

Here, the two self-energies are taken to be frequency dependent but momentum independent, and by using the formalism of Ref. 1, they become related through Δ_0, an important physical parameter of the theory:

$$\Psi(z) = -\frac{n^2}{4\Delta_0}\Phi(z). \tag{33}$$

The physical meaning of Δ_0 as the mean inelasticity of the auxiliary Fermi liquid (aux-FL) is emphasized in Ref. 1, and follows from Eq. (56). Thus $\rho_\Psi = -\frac{n^2}{4\Delta_0}\rho_\Phi$, and hence we get the simple result:[11]

$$G(\xi_k,z) = g(\xi_k,z)\left[\left(1-\frac{n}{2}\right) - \frac{n^2}{4\Delta_0}\Phi(z)\right]. \tag{34}$$

The auxiliary Fermi liquid has a Greens function $g^{-1}(\xi_k,z) = z - \xi_k - \Phi(z)$, where ξ_k is the electronic energy at wave vector k measured from the chemical potential μ, and therefore we may write the model Greens function as

$$G(\xi_k,z) = \frac{n^2}{4\Delta_0} + \left(\frac{n^2}{4\Delta_0}\right)\frac{\varepsilon_0 + \xi_k - z}{z - \xi_k - \Phi(z)}, \tag{35}$$

where

$$\varepsilon_0 = \Delta_0\,\frac{4}{n^2}\left(1-\frac{n}{2}\right). \tag{36}$$

With $\Gamma(x) = \pi\rho_\Phi(x)$, $\Re e\;\; \Phi(x+i0^+) = \mathcal{H}[\rho_\Phi](x)$ and $\varepsilon(\xi_k,x) \equiv [x - \xi_k - \mathcal{H}[\rho_\Phi](x)]$, we can express the spectral function and the real part of the Greens function as

$$\rho_G(\xi_k,x) = \left(\frac{n^2}{4\pi\,\Delta_0}\right)\frac{\Gamma(x)}{\Gamma^2(x)+\varepsilon^2(\xi_k,x)}\,(\varepsilon_0+\xi_k-x)\,, \tag{37}$$

$$\Re e\; G(\xi_k,x) = \left(\frac{n^2}{4\Delta_0}\right)\left[1 + \frac{\varepsilon(\xi_k,x)(\varepsilon_0+\xi_k-x)}{\Gamma^2(x)+\varepsilon^2(\xi_k,x)}\right]. \tag{38}$$

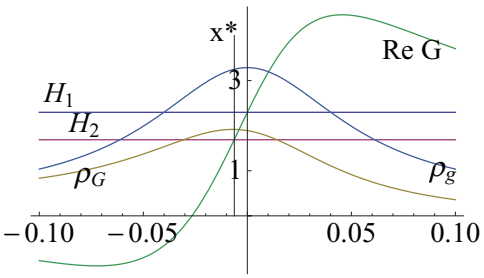

FIG. 1. (Color online) The density $n = 0.85$, temperature $T = 600$ K, $\Delta_0 = 0.0786$, and parameters are set I of Eq. (54). At this rather high temperature, we can see the details of the spectral shape clearly. The vertical line is at $x^* = E^*_{k_F}$, this energy is the location of the peak of the physical spectral function ρ_G as marked. Its leftward (i.e., red) shift relative to the Fermi-liquid peak at the chemical potential is clearly seen. The two horizontal lines specify the magnitude of the $\Re e\; G(0,x)$ at $x = 0$ (H1) and $x = E^*_{k_F}$ (H2). The line H1 is at height $n^2/(4\Delta_0)$ and H2 is at height $n^2/(4\Delta_0)(1 - Z_k/2)$.

The linear-frequency term in braces in Eq. (37) is termed the caparison factor in Ref. 1 and leads to significant features of the spectrum as discussed below. For completeness, we note the auxiliary Fermi-liquid part of the problem as

$$\rho_{\mathbf{g}}(\xi_k,x) = \frac{1}{\pi}\,\frac{\Gamma(x)}{\Gamma^2(x)+\varepsilon^2(\xi_k,x)}. \tag{39}$$

In Fig. 1, we plot the above three functions for a model system described more fully in Sec. IV F.

D. EDC or constant-wave-vector scans and energy dispersion

We first study the peak structure corresponding to fixing $\vec{k}$ the wave vector and hence ξ_k, and sweeping the energy x. These give rise to the energy distribution curves, i.e., the EDC's. The aux-FL part has a peak at $x = E_k^{\rm FL}$ for a given ξ_k, as in standard FL theory from solving for the roots of Eq. (31). For $k \sim k_F$, we find $E_k^{\rm FL} = \xi_k Z_k$ with the momentum-independent self-energy $\Phi(z)$, where

$$Z_k = \lim_{x\to E_k^{\rm FL}} [1 - \partial\;\Re e\Phi(x)/\partial x]^{-1}. \tag{40}$$

Expanding around this solution, we write

$$\varepsilon(\xi_k,x) \sim \frac{1}{Z_k}(x - Z_k\;\xi_k). \tag{41}$$

We will also write $\Gamma_k \equiv \Gamma(x)/_{x\to E_k^{\rm FL}}$ at the FL quasiparticle location, where we expect for the Fermi liquid $\Gamma_k \sim c_1(k - k_F)^2 + c_2T^2$, with suitable values as described more fully in Sec. IV F). At this value, we have the identity $\Re e\; G(\xi_k, E_k^{\rm FL}) = n^2/(4\Delta_0)$ as remarked above. As a consequence, in Fig. 1 the intersection of the line H1 and the vertical y axis also coincides with the value of $\Re e\; G$ at the chemical potential. To elucidate the line shape of the ECFL, we start with the FL solution and perturb around it to find the corrected location of the peaks in the full spectral function.

$$\rho_G^{\rm Peak}(\xi_k,x) = \frac{1}{\pi}\,\frac{Z_k^2\,\Gamma_k}{Z_k^2\,\Gamma_k^2 + \left(x - E_k^{\rm FL}\right)^2}\,\frac{n^2}{4\Delta_0}\,(\varepsilon_0+\xi_k-x). \tag{42}$$

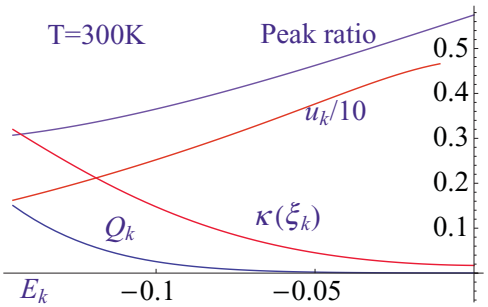

FIG. 2. (Color online) The density $n = 0.85$, $T = 300$ K, $\Delta_0 = 0.0678$, and parameters are from set I in Eq. (54). The various dimensionless variables shown against $E_k^{\rm FL}$ are the peak ratio from Eq. (50), the variable u_k (scaled by ten) from Eq. (44), the skew asymmetry factor $\kappa(\xi_k)$ from Eq. (65), and the variable Q_k from Eq. (61).

Similarly, the real part is found:

$$\Re e\, G^{\rm Peak}(\xi_k,x) = \frac{n^2}{4\Delta_0}\left[1 + Z_k \frac{(x - E_k^{\rm FL})(\varepsilon_0 + \xi_k - x)}{Z_k^2\,\Gamma_k^2 + \left(x - E_k^{\rm FL}\right)^2}\right]. \tag{43}$$

We introduce the following convenient positive variable u_k:

$$\sinh u_k \equiv \frac{\varepsilon_0 + \xi_k - E_k^{\rm FL}}{Z_k \Gamma_k}, \tag{44}$$

so that near the Fermi energy and at low T the small $\Gamma_k \sim T^2$ drives it to a large and positive value, i.e., $\exp u_k \to 1/T^2$. At higher binding energies, u_k decreases toward zero, as discussed below. We will also define a dimensionless variable Q_k below in Eq. (61) that depends on u_k only and determines the shape of the peak. To analyze the shape at a given ξ_k, we introduce a dimensionless energy variable ϵ through the relation

$$x = E_k^{\rm FL} + Z_k \Gamma_k\, \epsilon, \tag{45}$$

where we must require that $|\epsilon| \sim 1$ for the expansion around the FL peak to be valid. The spectral function is expressible as

$$\rho_G^{\rm Peak}(\xi_k,\epsilon) = \rho_G^*(k)\left[\frac{\sinh(u_k) - \epsilon}{1 + \epsilon^2}\right] 2e^{-u_k}, \tag{46}$$

$$\Re e\, G^{\rm Peak}(\xi_k,x) = \frac{n^2}{4\Delta_0}\left\{1 + Z_k\, \epsilon\, \frac{[\sinh(u_k) - \epsilon]}{1 + \epsilon^2}\right\}. \tag{47}$$

From Eq. (46) we see that at any k, the spectral function peaks at $\epsilon^* \equiv -e^{-u_k}$ with the true quasiparticle peak E_k^* corrected from the Fermi-liquid value $E_k^{\rm FL}(= Z_k\ \xi_k)$ as $E_k^* \equiv E_k^{\rm FL} - e^{-u_k} Z_k \Gamma_k$ at $\epsilon^* = -e^{-u_k}$. Simplifying, we find the EDC energy dispersion or spectrum

$$E_k^* = \xi_k + \varepsilon_0 - \sqrt{[\varepsilon_0 + (1 - Z_k)\,\xi_k]^2 + Z_k^2 \Gamma_k^2}\quad . \tag{48}$$

We provide examples of this dispersion later in Fig. 5.

For a given ξ_k, the magnitude of the spectral function at this peak is given by

$$\Re e\, G^*(k) = \frac{n^2}{4\Delta_0}\left(1 - \frac{1}{2}Z_k\right),$$
$$\rho_G^*(k) = \frac{n^2\, Z_k}{8\pi\,\Delta_0} e^{u_k}. \tag{49}$$

The magnitude of $\Re e\, G^*(k)$ is a little smaller than the value $n^2/(4\Delta_0)$ arising at the FL solution $\epsilon = 0$. In Fig. 1, this is reflected in the line H2 that lies a little below H1.[14]

The peak value $\rho_G^*(k)$ falls off with $\xi_k \ll 0$, and is always smaller relative to the peak of the aux-FL peak value $\rho_g^*(k)$. The ratio of the two peak values is given by

$$\frac{\rho_G^*(k)}{\rho_g^*(k)} = \frac{n^2\ Z_k \Gamma_k}{8\Delta_0} e^{u_k}. \tag{50}$$

We see below numerical examples of these functions. Figure 2 illustrates the peak ratio and other features for a typical set of parameters.

E. MDC or constant-energy scans and energy dispersion.

It is also useful to study the momentum distribution curves obtained by fixing the energy x and scanning the energy ξ_k.[15] In the model of a $\vec{k}$-independent self-energy, this is a particularly convenient strategy, and hence maximizing Eq. (37) at a fixed x, we find the MDC energy dispersion or spectrum:

$$\xi^*(x) = x - \varepsilon_0 + \sqrt{\Gamma^2(x) + [\varepsilon_0 - \Re e\Phi(x)]^2}. \tag{51}$$

Thus $\xi^*(x)$ is the peak position of ξ_k in constant-energy scans, whereas E_k^* in Eq. (48) represents peak position of energy at a fixed ξ_k. It is amusing to compare this with Eq. (48). Unlike Eq. (48), this formula is valid at all energies, not just near the chemical potential where the two agree closely. We will see below in Fig. 5 that this function is multivalued in a range of values of energy x leading to characteristic features of the spectrum.

F. Numerical example of highdimensional ECFL model

In this section, we use a rectangular band with height $1/(2W)$ and width $2W$, and take $W = 0.86$ eV (i.e., 10^4 K) as a typical value. In Ref. 3, a more realistic band structure is used as described in detail there. The model for the Fermi liquid introduced in Ref. 1 [see Eq. (24)] is given by the expression

$$\Gamma(x) = \pi\rho_\Phi(x) = \pi C_\Phi(x^2 + \tau^2)e^{-C_\Phi(x^2+\tau^2)/\omega_c} + \eta, \tag{52}$$

with $\tau = \pi k_B T$. We have added a scattering width η as in Ref. 3, in order to account for scattering by off planar impurities. The real part of the self-energy is found from the Hilbert transform of $\rho_\Phi(x)$, and is given by

$$\Re e\Phi(x) = C_\Phi \pi (x^2 + \tau^2)e^{-C_\Phi(x^2+\tau^2)/\omega_c} \times \mathrm{Erfi}(x/\sqrt{\omega_c}) - C_\Phi\ x\ \sqrt{\pi\omega_c}\ e^{-C_\Phi\tau^2/\omega_c}, \tag{53}$$

where $\mathrm{Erfi}(x) = \frac{2}{\sqrt{\pi}}\int_0^x e^{t^2}\,dt$ is the imaginary error function. A numerically small correction arising from η is dropped for brevity.

G. Typical parameters

The same model is also used in the fit to experiments in Ref. 3 with a slight change of notation given by writing $C_\Phi \to \frac{1}{\pi\Omega_0}$ and $\omega_c \to \frac{\omega_0^2}{\pi\Omega_0}$, in terms of the high- and low-frequency cutoff frequencies ω_0 and Ω_0. We use two sets of standard

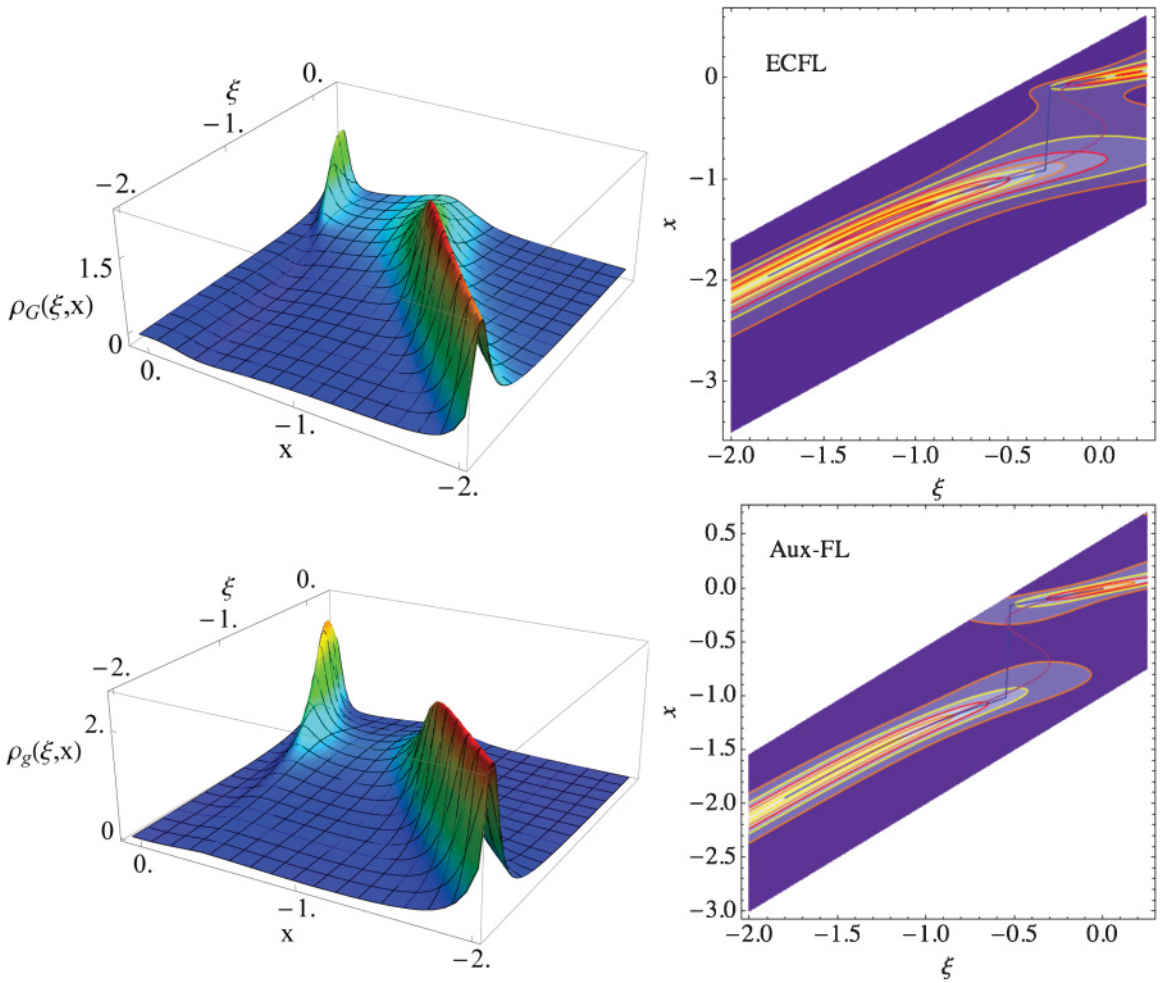

FIG. 3. (Color online) The ECFL (top left) and the auxiliary FL spectral functions (bottom left) at density $n = 0.85$, $T = 180$ K, $\Delta_0 = 0.12$ eV, $\eta = 0.12$ eV, and the other parameters are from Set II in Eq. (54). Here, ξ and x are in units of eV. In the ECFL curve on left, it is seen that the excitations near the Fermi energy become broad and dissolve into the continuum at an energy ~ -0.2 eV, and reappear as sharp modes at a deeper binding energy. In the auxiliary FL, the excitations near the Fermi energy remain sharp and extend to lower energies than in the ECFL curves. The contour plots of the same functions in the right panel (top ECFL and bottom auxiliary FL) give a complementary perspective of the spectrum. The two superimposed solid lines at top right are from curves I and II of Fig. 5 and at bottom right curves III and IV of Fig. 5.

parameters;

$$\begin{aligned} \text{Set I:}\quad & C_\Phi = 1\ \text{eV}^{-1},\quad \omega_c = 0.25\ \text{eV}\quad \text{or} \\ & \omega_0 = 0.5\ \text{eV},\ \ \Omega_0 = 0.318\ \text{eV} \\ \text{Set II:}\quad & C_\Phi = 2.274\ \text{eV}^{-1},\quad \omega_c = 0.568\ \text{eV}\quad \text{or} \\ & \omega_0 = 0.5\ \text{eV},\ \ \Omega_0 = 0.14\ \text{eV}. \end{aligned} \tag{54}$$

Set I was used in Ref. 1 for schematic plots employing a simple band density of states $g_B(\varepsilon) = \frac{1}{2W}\Theta(W^2 - \varepsilon^2)$. Set II was used in Ref. 3 employing a more elaborate dispersion described therein to successfully fit data on various high-temperature superconductors at optimal doping. The value of η is displayed in different plots. In Eq. (39), the spectral function ρ_g of the aux-FL is defined. The chemical potential is fixed by the number sum rule with $\xi = \epsilon - \mu$

$$\frac{n}{2} = \int_{-\infty}^{\infty} dx\ f(x) \int d\epsilon\ g_B(\epsilon)\, \rho_{\mathbf{g}}(\epsilon - \mu, x), \tag{55}$$

where $f(x) = (1 + e^{\beta x})^{-1}$ is the Fermi function. We now write the contributions from extreme correlations that are described in Ref. 1. The inelastic energy scale Δ_0 is found from the sum rule:

$$\Delta_0 = \int_{-\infty}^{\infty} dx\ f(x) \int d\epsilon\ g_B(\epsilon)\, \rho_{\mathbf{g}}(\epsilon - \mu, x)\, (\epsilon - \mu - x). \tag{56}$$

Thus at a given density and temperature n, T, the model has only two parameters ω_c and C_Φ so that Δ_0 is fixed from Eq. (56). We study the details of the spectra next.

V. THE SPECTRAL CHARACTERISTICS OF THE HIGH-DIMENSIONAL ECFL MODEL (37)

A. Global view of the spectral function

We display in Fig. 3 the spectral function for the ECFL model Eq. (37) in three-dimensional (3D) plots and contour plots. Two distinct perspectives of the spectrum are found in the figure from the 3D and the contour plots. In both of these plots, we see that the excitations are sharply defined only for

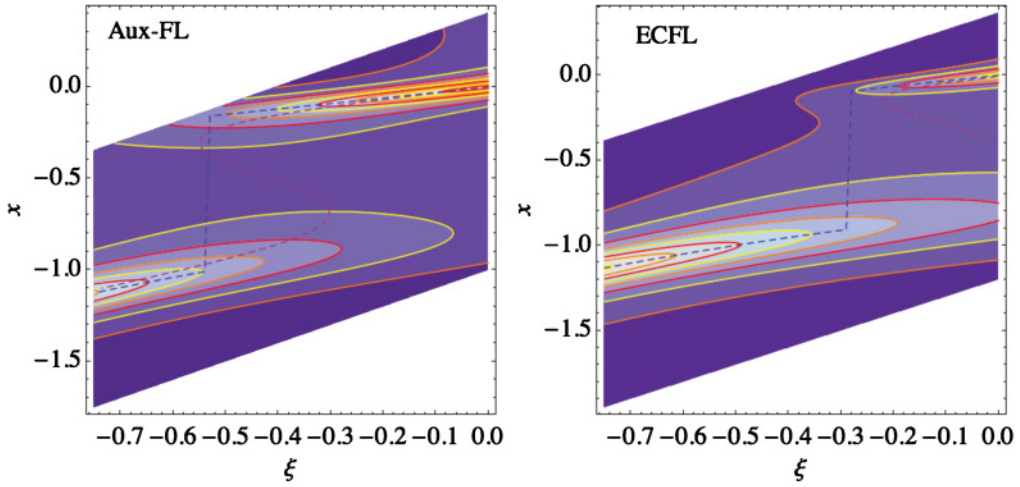

FIG. 4. (Color online) The contour plots of the aux-FL (left) and the ECFL model from Fig. 3 (right) with the same parameters as in Fig. 3 but over a smaller energy window. We superimpose the constant-wave-vector dispersion and MDC dispersion, with a value of $\eta = 0.12$ common to the contour plots. The energy scale of the feature near the chemical potential is considerably reduced in the ECFL, and the "jump" in the EDC dispersion occurs at roughly half the corresponding energy in the aux-FL.

a certain range near the Fermi energy, and then merge into the continuum. At higher binding energies, the spectrum again looks quite sharp. For comparison, in Fig. 3, we also display the aux-FL spectral function. We note that the aux-FL spectra also become sharp at higher binding energies. This sharpening is modeled by the Gaussian in Eq. (39), its basic origin is the decrease in the weight of physical processes capable of quasiparticle damping as we move toward the band bottom. In order to look more closely at the low-energy part of the spectrum of the aux-FL and the ECFL, we show in Fig. 4 the contour plots of both over a smaller energy range.

We see that viewed in this rather broad sense, dispersions of the aux-FL and the model ECFL spectra share many characteristics, with somewhat different energy scales. However, there are crucial differences that emerge when we look at the distribution of spectral weight that arises in the ECFL, where the caparison factor in Eq. (37) pushes weight to higher binding energies. This is reflected most significantly in the line shapes that we study below. Since we use the momentum-independent self-energy for the aux-FL in this model calculation, we obtain very detailed EDC and MDC plots below. However, it must be borne in mind that refined calculations within the ECFL framework must necessarily introduce some momentum dependence, and hence several details are likely to change, in particular the structure far from the chemical potential would change somewhat more. Our view is that, this caveat apart, it is very useful to take the Eq. (37) seriously since it gives a simple framework to correlate different data.

B. Dispersion relations in EDC and MDC

In Fig. 5, the EDC dispersion relation (i.e., locus of peaks of the spectral function at fixed ξ, found by numerical maximization), is plotted versus ξ along with the MDC spectrum Eq. (51). We recall that the latter expression is exact at all ξ and x, whereas Eq. (48) is not quite exact for the EDC dispersion. For comparison, we also show the corresponding figures for the aux-FL spectral function in Eq. (39), with the same parameters. The dispersion relations Eq. (48) is displayed in the inset of Fig. 5, where it is compared with the result of numerically maximizing the spectral function at a fixed ξ. We see that Eq. (48) is only good for a range of energies near the Fermi energy.

We see that both sets of spectra for the aux-FL as well as the ECFL model exhibit similar global features, but with different scales of energy. In both cases, the constant energy scans show a jump discontinuity, whereas the MDC spectra show an "S" type or re-entrant type behavior. The origin of the latter is easy to see in the aux-FL, here a peak in $-\Re e\Phi(x)$ occurs at an energy approximately $2\omega_0$, so that as x decreases from zero, $\xi^*_{\text{aux}-\text{FL}} = x - \Re e\Phi(x)$ goes back up for a certain range. In the case of the ECFL, Eq. (51) shows that the energy scale ε_0 enters the expression when $\Gamma(x)$ becomes comparable to $\varepsilon_0 - \Re e\Phi(x)$, and the net result is that the re-entrant behavior is pushed to lower binding energies.

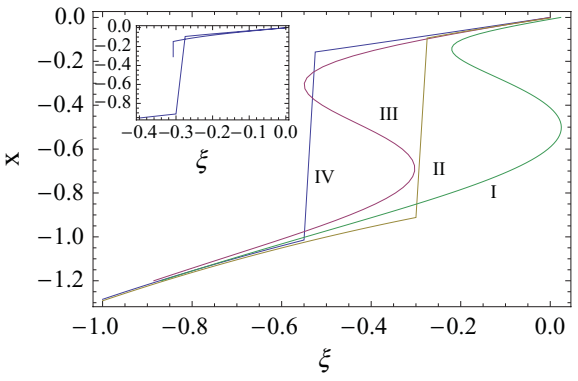

FIG. 5. (Color online) Energy dispersion curves in the ECFL and the aux-FL models. Here, the parameters are from set II in Eq. (54), with $n = 0.85$ and $T = 180$ K. With $\eta = 0.12$, curves I and II have the peaks in constant-wave-vector and constant-energy scans of the spectral function (37), and curves III and IV are corresponding figures for the aux-FL in Eq. (39). The inset compares Eq. (48) (the truncated curve) with the exact locus found by numerical maximization.

C. The energy shift

The dispersion (48) corresponds to the ridge near the Fermi energy in Fig. 3. At low temperature, since $\Gamma_{k_F} \sim O(T^2)$, the corrected quasiparticle energy is always less than $E_k^{\rm FL}$, so that there is always a leftward (i.e., red) shift of the dispersion, or from the hole (binding) energy point of view, we may say there is a blue shift. The peak shift is given by

$$\Delta E_k = E_k^* - E_k^{\rm FL} = (1 - Z_k)\xi_k + \varepsilon_0 - \sqrt{[\varepsilon_0 + (1 - Z_k)\,\xi_k]^2 + Z_k^2\Gamma_k^2}, \tag{57}$$

which is a function of both T and k. Close to the Fermi energy, this can be written as

$$\Delta E_k = -\frac{Z_{k_F}^2\,\Gamma_k^2}{2\varepsilon_0}. \tag{58}$$

At the Fermi momentum, this small shift is seen in Fig. 1 where the vertical line through x^* is displaced to the left from the y axis. As long as $k \sim k_F$ this shift is very small $\Delta E_k \sim O(T^4)$, but as k moves away from k_F the shift (57) grows with ξ_k. This departure makes the dispersion in Eq. (48) depart significantly from the bare dispersion ξ_k as we move away from k_F. We see from Fig. 5 that the departure of the EDC peaks from the Fermi liquid is somewhat less pronounced than those of the MDC's, the latter is operationally called the low-energy kink. Our calculations therefore predict the magnitude of the shift (57) in terms of the energy scale ε_0 and the Fermi-liquid parameter Γ_k. This energy shift is therefore also a useful method for extracting the fundamental parameter Δ_0 on using Eq. (36).

D. Constant-energy cuts or MDC line shapes

We display the MDC line shapes in Fig. 6. Panel (a) shows the effect of the caparison factor $[1 - \frac{n}{2} + \frac{n^2}{4\Delta_0}(\xi - x)]$, whereby the curves are skewed to the right, in contrast to the EDC curves that are skewed to the left. The latter important feature is also seen below in Fig. 7(a) and noted in Ref. 1. Panel (b) shows the shallow peaks in the "S-like" region of the energy dispersion seen in Fig. 5, and panel (c) shows the deep interior region where the peaks are more symmetric.

E. Constant wave-vector cuts or EDC line shapes

The spectral function and the real part of the Greens function are calculated from Eqs. (38) and (37). We display the EDC line shapes in Fig. 7. Panel (a) gives an overview of the spectral shapes for wave vectors near the Fermi surface, displaying a left skewed peak that falls rapidly in intensity as it broadens. This behavior is of great interest since it captures the experimental features in high$-T_c$ systems, as elaborated in Ref. 3. Panel (b) shows the spectra at higher binding energies, where a feature at lower energies begins to disperse significantly with ξ. It is evident that these two sets of dispersing features correspond to the two branches that are seen in the 3D plots and contour plots of Fig. 3. The inset in Fig. 7(b) shows the behavior of the aux-FL, where the two features are again seen but with different rates of intensity change.

We now turn to the task of understanding the reconstructed Dyson self-energy that leads to the above electron spectral functions. In Fig. 8, we show the spectral function ρ_G at various values of the energy ξ at $T = 300$ K. The Fermi-liquid spectra at the same values of parameters are also shown for comparison. The Dyson self-energy $\rho_\Sigma(\xi,x)$ necessary to produce these spectral functions is found using Eq. (23) and is displayed in Fig. 8 at two temperatures. The object $\rho_\Sigma(\xi,x)$ has a distinctive minimum for each ξ that shifts to the left along with the energy ξ, which tracks the peaks in the physical spectral function $\rho_G(\xi,x)$ from Eq. (23). It also shows the asymmetry between energies above and below the chemical potential that we noted at $\xi = 0$ in Fig. 9. At the Fermi energy, $\rho_\Sigma(\xi,x)$ is displayed in Fig. 9 over a large scale.

F. The reduced line-shape function

An interesting aspect of the ECFL model Greens function (37) is the change in shape of the peaks as we leave the Fermi surface, so that the quasiparticles become hard to define at some point. This change in shape can be formulated neatly in terms of a single dimensionless parameter Q_k that we now define and explore. We examine Eq. (46) around its peak by writing

$$\epsilon = \epsilon^* + \cosh(u_k)\bar{\epsilon}, \tag{59}$$

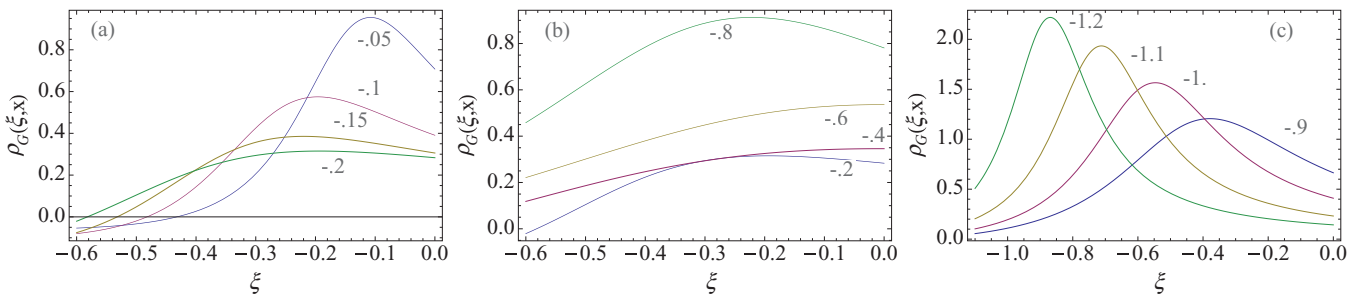

FIG. 6. (Color online) MDC line shapes at different values of energy x displayed in each curve. Here, the parameters are from set II in Eq. (54), with $n = 0.85$, $T = 180$ K, and $\eta = 0.12$. Panel (a) corresponds to x close to the chemical potential. It is interesting to note that the curves are skewed to the right, thus mirror imaging the leftward skew seen in the constant-ξ (EDC) scans below Fig. 7(a), in a comparable range of energies and wave vectors. Panel (b) corresponds to the midenergy range, within the reentrant range of x from Figs. 5 or 3, with the counterintuitive movement of the shallow peak to the right with increasing x. Panel (c) corresponds to the second set of maxima in Fig. 3 far from the chemical potential, where the curves are quite symmetric.

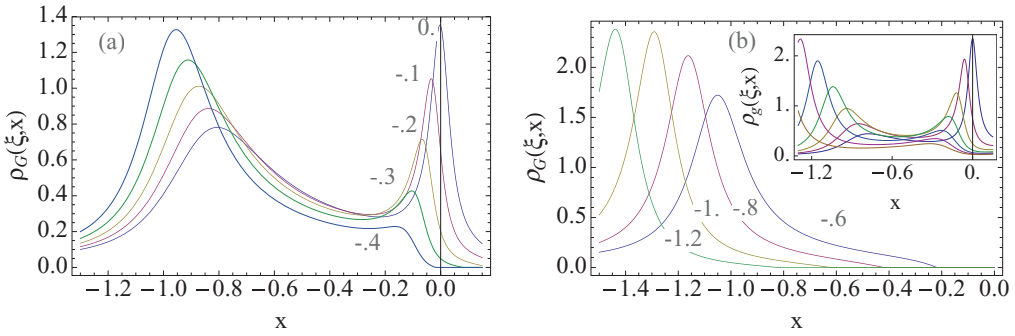

FIG. 7. (Color online) EDC line shapes at different values of energy ξ displayed in each curve. Here, the parameters are from set II in Eq. (54), with $n = 0.85$, $T = 180$ K, and $\eta = 0.12$. Panel (a) corresponds to ξ close to the chemical potential. Note that the curves are skewed to the left, i.e., a mirror image of the rightward skew seen in the constant-x MDC scans above Fig. 6, in a comparable range of energies and wave vectors. Panel (b) corresponds to the higher energy range, and we see that only one broad maximum is found at a given ξ. The inset in (b) shows the aux-FL constant-ξ scans for the same range; here, each ξ results in a pair of maxima, originating from the functional form of the self-energy in Eq. (37).

so that $\rho_G^{\rm Peak}(\xi_k,\bar{\epsilon}) = \rho_G^*(k)\gamma(Q_k,\bar{\epsilon})$, with a characteristic lineshape function γ given by

$$\gamma(Q_k,\bar{\epsilon}) = \left[\frac{Q_k(1-\bar{\epsilon})}{Q_k(1-\bar{\epsilon})+\bar{\epsilon}^2}\right], \tag{60}$$

with

$$Q_k = 2\frac{e^{-u_k}}{\cosh(u_k)}. \tag{61}$$

The parameter Q_k goes to zero near the Fermi surface at low T since $u_k \to \infty$, but at higher binding energies increases: $Q_k \to 2$.

As we get deeper into the occupied states $\xi \ll 0$, we find a remarkable change in shape of the spectral functions. This is illustrated in Fig. 10 where we plot γ of Eq. (60) after normalizing to unit area. In order to have a well-defined quasiparticle-type peak in ρ_G for $\epsilon \sim O(1)$, Q_k must be small enough. This translates to the requirement of ξ_k being close to the Fermi surface. By setting $Q \sim 1$ as the condition for losing a peak in the spectrum, we obtain the condition

$$\varepsilon_0 + (1-Z_k)\xi_k = \frac{1}{\sqrt{3}}Z_k\Gamma_k, \tag{62}$$

beyond which it is meaningless to talk of quasiparticles. This gives ε_0 as a rough characteristic scale for the disappearance of the quasiparticle peaks.

Figure 11 illustrates the change in shape somewhat differently by normalizing all curves to unity at the peak as in Eq. (60). The peak at $\bar{\epsilon} = 0$ is sharp and quite symmetric for $Q \ll 1$, and becomes broader and more left skewed as Q_k increases toward its maximum value of two. Attaining the maximum value is possible, in principle, requirement being $u_k = 0$ or from Eq. (44):

$$\Delta_0 = \frac{n^2}{4-2n}\,\Re e\,\Phi\big(E_k^{\rm FL}\big). \tag{63}$$

Unless Δ_0 is very small, this condition is hard to satisfy. If this possibility is achieved, then there are several interesting consequences. Firstly, we note that from Eq. (49), the magnitude of the spectral function at $u_k = 0$ becomes insensitive to disorder and temperature, etc. Its magnitude, $n^2 Z_k/(8\pi\Delta_0)$, should be useful for finding Δ_0. If this is approximately satisfied, then the peak structure loses meaning and the spectrum is essentially flat. Taking $\bar{\epsilon} = -1$, the fall off from the peak value of unity is 80%, and the spectrum becomes essentially featureless.

G. Skewness parameter of the spectrum

We now estimate the skewness of the spectrum. The function (60) drops to half its peak value at two values of $\bar{\epsilon}_{L,R}$ to the left and right of the peak given by

$$\bar{\epsilon}_{L,R} = -\tfrac{1}{2}Q_k \mp \sqrt{Q_k + \tfrac{1}{4}Q_k^2}. \tag{64}$$

For small $Q \ll 1$, the (dimensionless) width of the peak is small, it increases with Q as discussed further below. We define a dimensionless skew parameter in terms of the energies $\epsilon^*,\epsilon_{R,L}$ [rather than the $\bar{\epsilon}$'s that are related via Eq. (59)]:

$$\kappa(\xi_k) = \frac{2\epsilon^* - \epsilon_R - \epsilon_L}{\epsilon^* - \epsilon_L} = \tanh(u_k) - 1 + \sqrt{[2-\tanh(u_k)]^2 - 1}, \tag{65}$$

with the property that near the Fermi level when $u_k \to +\infty$ the variable $\kappa \to 0$, and we get a symmetric curve about the maximum. On the other hand, for deeper occupation, u_k decreases in magnitude toward zero, driving $\kappa \to 0.732$ and gives a curve that is increasingly biased to the left. The asymmetry κ grows as $O(T^2)$ at low temperatures, and it is rather large at room temperature. As a rough estimate, the quasiparticle peak is lost when $Q_k \sim 0.5$ where $u_k \sim 0.98$ and $\kappa(\xi_k) \sim 0.5$. This loss of quasiparticle peak structure, skew factor, and its experimental signature is studied in greater detail in Ref. 3. See Fig. 2 for typical plot of skew parameter κ and Q versus the hole binding energy E_k.

VI. SELF-ENERGY OF THE SELF-ENERGY AND A MORI-TYPE PROCEDURE.

Since the construction given above generates $\Sigma(z)$ from $G(z)$ given only the representation (1), we can as well repeat the trick. Since $\Sigma(z)$ satisfies Eq. (18) with a density $\rho_\Sigma(x)$ that is assumed known, and is analytic in the complex z plane

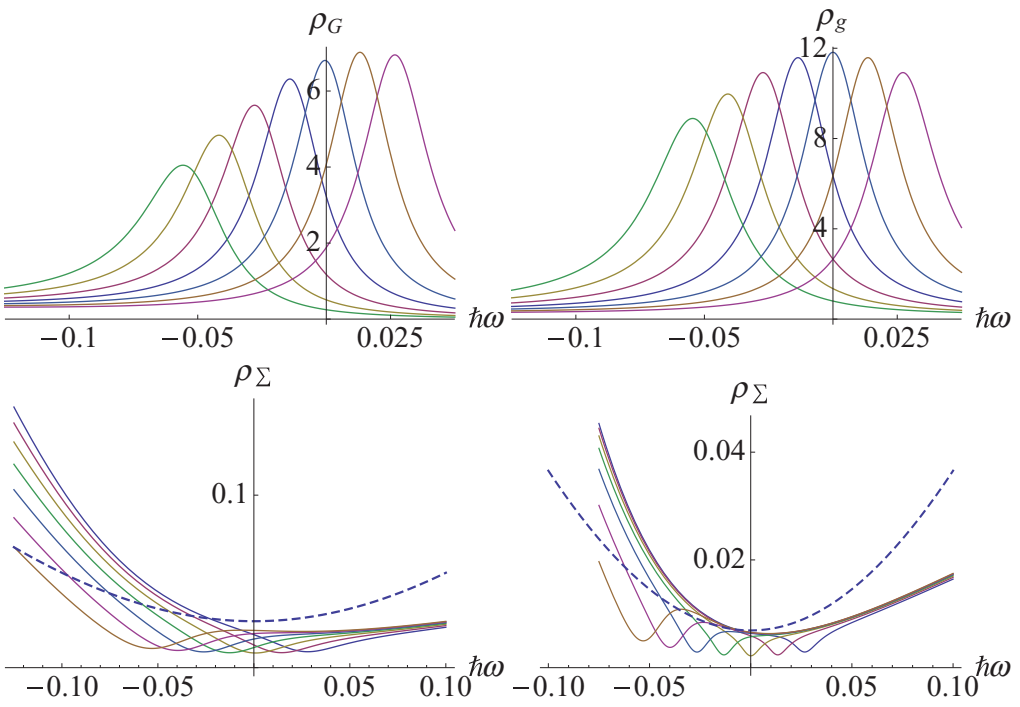

FIG. 8. (Color online) Top left panel: density $n = 0.85$, temperature $T = 300$ K, $\Delta_0 = 0.0678$, and other parameters are from set I in Eq. (54). From left to right $\rho_G(\xi,x)$ for energies in units of eV: $\xi = -0.1, -0.075, -0.05, -0.025, 0, 0.025, 0.05$. Top right panel: spectral function $\rho_g(\xi,x)$ from Eq. (39) corresponding to the same ξ as in the left panel. The difference in the line shapes becomes clear when we examine the Dyson self-energy that produces these curves. Bottom left panel: the panel shows the spectral function at $T = 300$ K for the inferred Dyson self-energy $\rho_\Sigma(x)$ from Eqs. (23), (38), and (37) for the same energies. The dashed line is the input Fermi-liquid spectral function $\rho_\Phi(\omega)$ at the same temperature. Bottom right panel: temperature $T = 150$ K, $\Delta_0 = 0.0642$, and the identical data as in the bottom left panel.

with a $1/z$ fall off, it satisfies the necessary conditions for a further decomposition. Consulting Eq. (23), we write down by inspection:

$$\Sigma(z) = \frac{a_\Sigma}{z - \bar{E}_\Sigma - \Sigma^{(1)}(z)},$$
$$\Sigma^{(1)}(z) = \int dx\ \frac{\rho_{\Sigma^{(1)}}(x)}{z - x}. \tag{66}$$

The constants $a_\Sigma = \int dx\ \rho_\Sigma(x)$ and $\bar{E}_\Sigma = \int dx\ x\rho_\Sigma(x)/a_\Sigma$ are known through $\rho_\Sigma(x)$. They may in practice be conveniently determined in terms of the moments of the Greens function[7–9] in applications. The spectral function is given by

$$\rho_{\Sigma^{(1)}}(x) = \frac{a_\Sigma\ \rho_\Sigma(x)}{[\pi^2\rho_\Sigma(x)]^2 + [\Re e\ \Sigma(x)]^2}. \tag{67}$$

Comparing this representation with Eq. (21), we note the formal similarity between $\rho_G(x)$ and $\rho_{\Sigma^{(1)}}(x)$. Thus for a Fermi liquid with momentum-independent self-energy, its

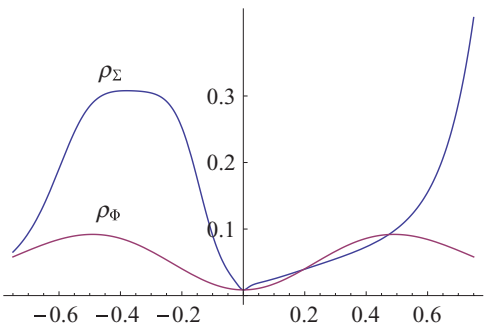

FIG. 9. (Color online) With $n = 0.85$ and $T = 300$ K, and the other parameters from set I in Eq. (54). The spectral function for the inferred Dyson self-energy $\rho_\Sigma(\xi = 0,x)$ using Eq. (23) and the the input Fermi-liquid spectral function $\rho_\Phi(x)$ over a larger energy range. Note the distinctive asymmetry in shape of ρ_Σ below and above the Fermi energy.

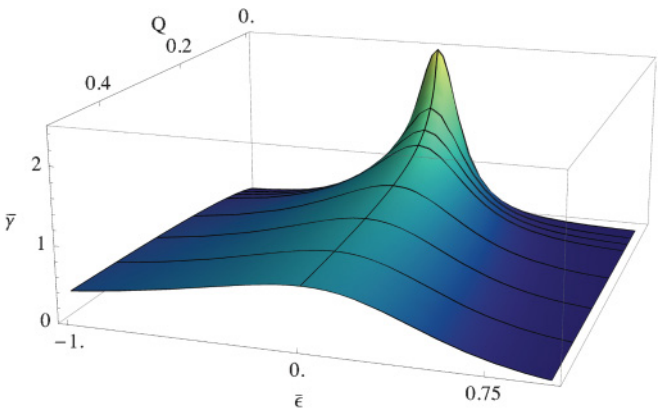

FIG. 10. (Color online) The spectral shapes possible are seen by plotting the shape function at different values of the parameter Q. In this curve, $\bar{\gamma}$ is the $\gamma(Q,\bar{\epsilon})$ of Eq. (60) normalized to unit area in the natural interval $[-1,1]$ for the variable $\bar{\epsilon}$.

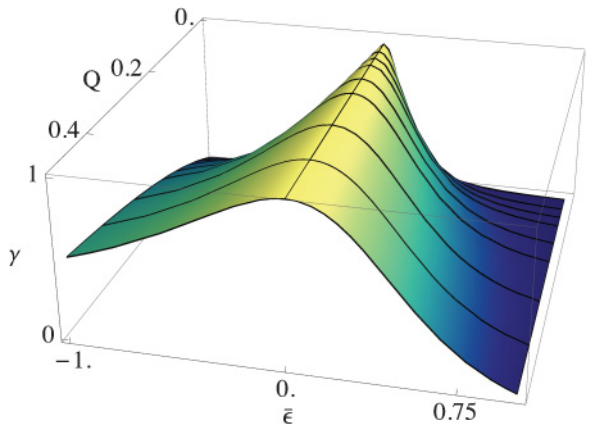

FIG. 11. (Color online) The same shapes as in Fig. 10 but now γ is normalized to unity at the peak as in Eq. (60). The sharp peaks for small $Q \leqslant 0.25$ flatten out as Q increases with a left skew asymmetry that is characteristic of this functional dependence.

next self-energy resembles closely the spectral function ρ_G, especially at the Fermi energy.

We follow up briefly on the above amusing observation, and obtain a hierarchy of self-energies starting from an initial self-energy given by the spectral representation, Eqs. (18) and (66). This process parallels the continued fraction representation of analytic functions and seems intimately related to the formalism developed by Mori.[7,8] The latter is expressed in the language of projection operators for Liouville operators that is less straightforward than our simple treatment.

In order to conform to the notation popular in the Mori formalism, we will express the variables in Laplace representation rather than the one used above with complex frequencies. Let us consider the thermal and temporal correlation function for two operators A and B in Schrödinger time and its Laplace transform:

$$C_{AB}(t) = \int_0^\beta d\tau\ \langle A(t - i\tau)B(0)\rangle,$$
$$\hat{C}_{AB}(s) = \int_0^\infty e^{-st}\ C_{AB}(t)\, dt. \tag{68}$$

In the standard case, we find $A = B^\dagger$, where the product is real and also positive.[16] We see that the Laplace-transform function satisfies an integral representation:

$$\hat{C}_{AB}(s) = \int_{-\infty}^{\infty} d\nu\ \frac{\rho_{AB}(\nu)}{s - i\nu}, \quad \text{with a real density given by}$$
$$\rho_{AB}(\nu) = \sum_{nm} \frac{p_m - p_n}{\varepsilon_n - \varepsilon_m} \langle n|A|m\rangle\ \langle m|B|n\rangle\ \delta(\varepsilon_n - \varepsilon_m - \nu). \tag{69}$$

This object is closely connected with the correlation functions used in Eqs. (1) and (2) by using the fluctuation-dissipation theorem. Following Mori, we write down a relaxation function with the normalization property $Z_0(0) = 1$, and its Laplace transform

$$Z_0(t) \equiv \frac{C_{AB}(t)}{C_{AB}(0)}, \quad \hat{Z}_0(s) = \int_{-\infty}^{\infty} d\nu\ \frac{\rho_0(\nu)}{s - i\nu}. \tag{70}$$

Here, the real density $\rho_0(\nu) = \frac{1}{C(0)}\rho_{AB}(\nu)$, satisfies the normalization condition $\int_{-\infty}^{\infty} d\nu\ \rho_0(\nu) = 1$. Using the identity

$$\frac{1}{0^+ + i(u - v)} = \pi\ \delta(u - v) - i\mathcal{P}\frac{1}{u - v},$$

with $\mathcal{P}$ denoting the principle value, an inverse relation expressing $\rho_0(\nu) = \frac{1}{\pi}\Re e\ \hat{Z}_0(0^+ + i\nu)$ follows. In order to find a Dyson-type representation for ρ_0, following Eqs. (8) and (9), we take the "equation of motion" by multiplying Eq. (70) by s and write

$$s\hat{Z}_0(s) = 1 + i \int_{-\infty}^{\infty} d\nu\ \frac{\nu\ \rho_0(\nu)}{s - i\nu} \equiv Y_0(s)\ \hat{Z}_0(s). \tag{71}$$

The Dyson form of self-energy now emerges and we obtain

$$\hat{Z}_0(s) = \frac{1}{s - iY_0(s)}, \quad \text{with} \quad Y_0(s) = \frac{\int_{-\infty}^{\infty} d\nu\ \frac{\nu\ \rho_0(\nu)}{s - i\nu}}{\int_{-\infty}^{\infty} d\nu\ \frac{\rho_0(\nu)}{s - i\nu}}. \tag{72}$$

As $s \to \infty$, the function $Y_0(s)$ tends to ω_1, with a real frequency ω_1 given by

$$\omega_1 = \int_{-\infty}^{\infty} d\nu\ \nu\ \rho_0(\nu). \tag{73}$$

Hence the function $Y_0(s) - \omega_1$ falls off as $1/s$ as $s \to \infty$. It is analytic everywhere except on the imaginary s axis. It therefore has a representation

$$Y_0(s) - \ \omega_1 = i\ \alpha_1 \int_{-\infty}^{\infty} d\nu\ \frac{\rho_1(\nu)}{s - i\nu}, \tag{74}$$

with a real density $\alpha_1\rho_1(\nu) = \frac{1}{\pi}\Im m[Y_0(0^+ + i\nu)]$. With this, we may write

$$Z_0(s) = \frac{1}{s - i\ \omega_1 + \alpha_1 \int\ d\nu\ \frac{\rho_1(\nu)}{s - i\nu}}. \tag{75}$$

The real number α_1 is found using the convention that $\rho_1(\nu)$ is normalized to unity. We may express ρ_1 solely in terms of the lower density $\rho_0(\nu)$ by using Eq. (70) as

$$\alpha_1\rho_1(u) = \frac{\rho_0(u)}{\pi^2\rho_0^2(u) + [\mathcal{H}[\rho_0](u)]^2}. \tag{76}$$

We determine α_1 from Eq. (76) by integrating over ν and using the unit normalization of $\rho_1(u)$. It is evident from Eq. (76) that for the physically important case of a real and positive initial density $\rho_0(\nu)$, the derived density $\rho_1(\nu)$ is also real positive.

This scheme is clearly generalizable to higher orders, and we simply iterate the above process. The answers may be written down by inspection as follows:

$$\hat{Z}_j(s) = \int_{-\infty}^{\infty} d\nu\ \frac{\rho_j(\nu)}{s - i\nu}, \quad \text{with normalization:}$$
$$\int_{-\infty}^{\infty} d\nu\ \rho_j(\nu) = 1. \tag{77}$$

These satisfy the recursion relation

$$\hat{Z}_j(s) = \frac{1}{s - i\ \omega_{j+1} + \alpha_{j+1}\ \hat{Z}_{j+1}(s)}, \tag{78}$$

where

$$\omega_{j+1} = \int_{-\infty}^{\infty} d\nu\ \nu\ \rho_j(\nu), \tag{79}$$

and α_{j+1} as well as $\rho_{j+1}(\nu)$ are defined through

$$\alpha_{j+1}\ \rho_{j+1}(u) = \frac{\rho_j(u)}{\pi^2\ \rho_j^2(u) + [\mathcal{H}[\rho_j](u)]^2}. \tag{80}$$

Note that the numbers α_j as well as ω_j are real, and for all j, the densities $\rho_j(\nu)$ are positive provided the the initial density $\rho_o(\nu)$ is positive. This situation arises when the initial operators $B = A^\dagger$, as mentioned above.

It is clear that Eq. (76) is the precise analog of the relation (23) for the Greens function. The hierarchy of equations consisting of Eqs. (45)–(49) constitutes an iteration scheme that starts with the $j = 0$ correlation function in Eq. (70). This is a forward hierarchy in the sense that successive densities at level $j + 1$ are expressed explicitly in terms of the earlier ones at level j. In the reverse direction, it is rather simpler since level j is explicitly given in terms of level $j + 1$ by Eq. (78). The use of this set of equations requires some *a priori* knowledge of the behavior of higher order self-energies to deduce the lower ones. Standard approximations[7] consist of either truncation of the series or making a physical assumption such as a Gaussian behavior at some level and then working out the lower level objects. Our object in presenting the above procedure is merely to point out that this iterative scheme is in essence a rather simple application of the self-energy concept described above, with the repeated use of Eq. (23).

VII. SUMMARY AND CONCLUSIONS

A new form of the electronic Greens function, departing widely from the Dyson form arises in the extreme correlation theory of the t-J model. Motivated by its considerable success in explaining ARPES data of optimally doped cuprate superconductors,[3] we have presented in this paper results on the detailed structure of this Greens function and its spectral function. An illustrative example is provided, complete with numerical results, so that the novel line shape and its dependence on parameters is revealed. We have also presented a set of explicit results on the Mori form of the self-energy that holds promise in several contexts.

ACKNOWLEDGMENTS

This work was supported by DOE under Grant No. FG02-06ER46319. I thank G-H. Gweon for helpful comments and valuable discussions. I thank A. Dhar and P. Wolfle for useful comments regarding the Mori formalism.

[1] B. S. Shastry, Phys. Rev. Lett. **107**, 056403 (2011).
[2] B. S. Shastry, Phys. Rev. B **81**, 045121 (2010).
[3] G.-H. Gweon, B. S. Shastry, and G. D. Gu, Phys. Rev. Lett. **107**, 056404 (2011).
[4] D. E. Logan, M. P. Eastwood and M. A. Tusch, J. Phys. Condens. Matter **10**, 2673 (1998).
[5] Z. Wang, Y. Bang, and G. Kotliar, Phys. Rev. Lett. **67**, 2733 (1991).
[6] J. M. Luttinger and J. C. Ward, Phys. Rev **118**, 1417 (1960); J. M. Luttinger, *ibid*. **119**, 1153 (1960); **121**, 942 (1961).
[7] H. Mori, Prog. Theor. Phys. **33**, 423 (1965); **34**, 399 (1965).
[8] M. Dupuis, Prog. Theor. Phys. **37**, 502 (1967).
[9] J. J. Deisz, D. W. Hess, and J. W. Serene, Phys. Rev. **55**, 2089 (1997).
[10] A. A. Abrikosov, L. Gorkov, and I. Dzyaloshinski, *Methods of Quantum Field Theory in Statistical Physics* (Prentice-Hall, Englewood Cliffs, NJ, 1963). Our $\rho_G(\xi_k,x)$ corresponds to the combination of spectral functions $A(\vec{k},x)$ and $B(\vec{k},x)$ used here.
[11] The positive part constraint on the right of the following equation can be often omitted, we found that it is violated very slightly ∼3% in many cases. We omit it for simplicity in the following.
[12] Shifting $\hat{E}$ by a constant is also possible but the optimal choice is the one made here.
[13] The notation is simplified from that in Ref. 1 by calling the extremely correlated Greens function as G rather than $\mathcal{G}$ and the overbar in the self-energy $\bar{\Phi}$ is omitted.
[14] At $T = 0$, this finite value persists and $\Re e G^{\rm Peak}[\xi_k, x^*(\xi_k)]$ does not diverge, so that one might be concerned that the Luttinger-Ward volume theorem is being disobeyed. In comparison, note that the standard FL Greens function behaves in a slightly different way, at any finite T and ξ_k, at the energy $x = E_k^{\rm FL}$ we find both a peak in the spectral function $\rho_g(\xi_k, E_k^{\rm FL})$ and a zero of the $\Re e g(\xi_k, E_k^{\rm FL})$, whereas at $T = 0$, we find a delta peak in the spectral function $\rho_g(\xi_k, E_k^{\rm FL})$ and a pole of the $\Re e g(\xi_k, E_k^{\rm FL})$. However we see that the FL divergence of the real part of G of a typical Fermi liquid does occur, but displaced by a very small energy scale $O(T^4)$. The peak positions are displayed in Fig. 1 at a high enough temperature so that the features are distinguishable.
[15] The process of scanning ξ_k used here differs slightly from the true MDC's, where one scans the wave vector $\vec{k}$ rather than the energy ξ_k, but is more convenient here.
[16] The spectral function $\rho_{AA^\dagger}(x)$ defined below in Eq. (69) is positive as well. However, that condition can be relaxed and we can do with less, provided that the spectral function in Eq. (69) is real (rather than positive). For this to happen, we may allow for $A \neq B^\dagger$, but in this case, assume that both the matrix elements $\langle nAm\rangle$ and $\langle mBn\rangle$ are real numbers or imaginary numbers so that the product is real. These conditions correspond to both operators A and B being Hermitian (or anti Hermitian), and the absence of magnetic fields so that the wave functions may be chosen to be real. Thus we will assume the reality of the product of the matrix elements.

Erratum: Anatomy of the self-energy [Phys. Rev. B 84, 165112 (2011)]

B. Sriram Shastry

(Received 2 August 2012; published 13 August 2012)

DOI: 10.1103/PhysRevB.86.079911 PACS number(s): 79.60.−i, 99.10.Cd

The spectral function $\rho_\Sigma(\omega)$ of the Dyson self-energy, inferred from Eq. (23), is incorrectly shown in the lower two graphs of Fig. 8 and in Fig. 9, due to an erroneous code. The corrected figures are provided; the captions and text remain unchanged.

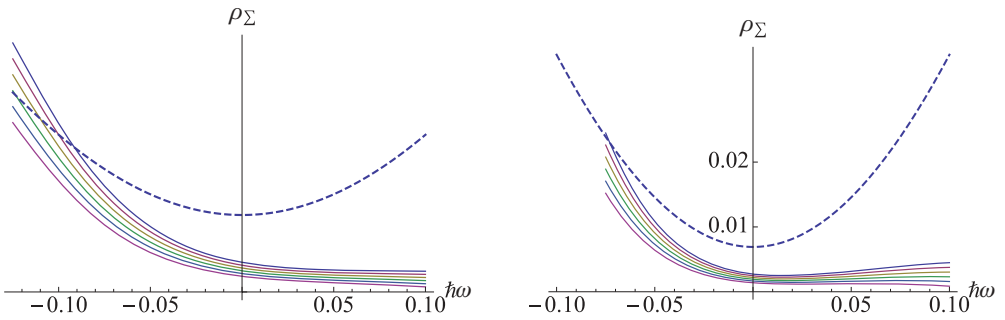

FIG. 1. (Color online) Replacement of lower panel in Fig. 8.

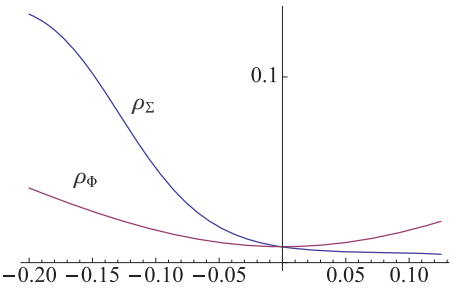

FIG. 2. (Color online) Replacement of Fig. 9.

